AIP | Journal of Applied Physics

Calculation of the spatial resolution in two-photon absorption spectroscopy applied to plasma diagnosis

M. Garcia-Lechuga, L. M. Fuentes, K. Grützmacher, C. Pérez, and M. I. de la Rosa

Citation: Journal of Applied Physics **116**, 133103 (2014); doi: 10.1063/1.4896497
View online: http://dx.doi.org/10.1063/1.4896497
View Table of Contents: http://scitation.aip.org/content/aip/journal/jap/116/13?ver=pdfcov
Published by the AIP Publishing

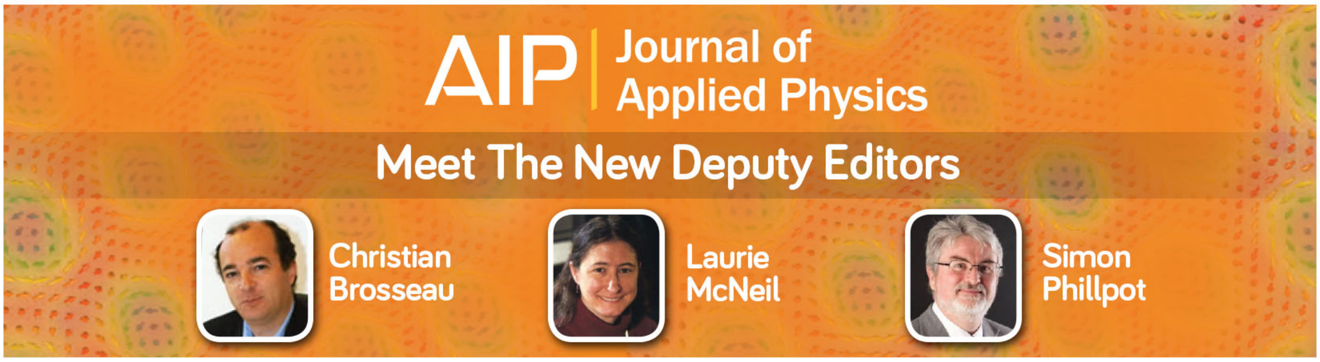

JOURNAL OF APPLIED PHYSICS **116**, 133103 (2014)

Calculation of the spatial resolution in two-photon absorption spectroscopy applied to plasma diagnosis

M. Garcia-Lechuga,[1,2] L. M. Fuentes,[3] K. Grützmacher,[1] C. Pérez,[1,a] and M. I. de la Rosa[1]
[1]*Departamento de Física Teórica, Atómica y Óptica, Universidad de Valladolid, 47011-Valladolid, Spain*
[2]*Laser Processing Group, Instituto de Óptica "Daza de Valdés," CSIC, 28006-Madrid, Spain*
[3]*Departamento de Física Aplicada, Universidad de Valladolid, 47011-Valladolid, Spain*

(Received 23 July 2014; accepted 14 September 2014; published online 3 October 2014)

We report a detailed characterization of the spatial resolution provided by two-photon absorption spectroscopy suited for plasma diagnosis via the 1S-2S transition of atomic hydrogen for optogalvanic detection and laser induced fluorescence (LIF). A precise knowledge of the spatial resolution is crucial for a correct interpretation of measurements, if the plasma parameters to be analysed undergo strong spatial variations. The present study is based on a novel approach which provides a reliable and realistic determination of the spatial resolution. Measured irradiance distribution of laser beam waists in the overlap volume, provided by a high resolution UV camera, are employed to resolve coupled rate equations accounting for two-photon excitation, fluorescence decay and ionization. The resulting three-dimensional yield distributions reveal in detail the spatial resolution for optogalvanic and LIF detection and related saturation due to depletion. Two-photon absorption profiles broader than the Fourier transform-limited laser bandwidth are also incorporated in the calculations. The approach allows an accurate analysis of the spatial resolution present in recent and future measurements. © *2014 AIP Publishing LLC*. [http://dx.doi.org/10.1063/1.4896497]

I. INTRODUCTION

Laser spectroscopic techniques became an important role in plasma diagnosis in the last 3 decades.[1,2] Among the large variety of laser aided plasma diagnostic methods, different two-photon spectroscopic techniques have been applied to miscellaneous plasmas far off thermodynamic equilibrium, because they provide several important advantages, like excitation from the ground state, high spatial and temporal resolution, Doppler-free and Doppler broadened measurements, etc., hence allow to determine plasma parameters not accessible by other means. The commonly applied detection scheme was direct or stepwise laser induced fluorescence (LIF), i.e., Ref. 3 and the references therein.

For many years our group, in close collaboration with Physikalisch Technische Bundesanstalt PTB (Berlin), has been involved in the development of two-photon spectroscopic techniques and high power UV-laser spectrometers, which provide single longitudinal mode radiation, necessary to benefit the great potential provided by two-photon spectroscopy. Two-photon polarization spectroscopy[4] allows for direct measurement of the two-photon absorption and was used for measuring Stark broadening 1S-2S hydrogen,[5] for the determination of atomic hydrogen densities in a stationary wall stabilized cascaded arc plasma,[6] in a hollow cathode discharge (HCD)[7] and in atmospheric pressure flames,[8] and for the determination of local electric field (E-field) strength[9] as well. Two-photon induced Lyman-α fluorescence was employed in feasibility study for tokamak diagnostic[10] and Balmer-α fluorescence for local E-field strength determination in an optogalvanic cell.[11] All of these methods provided high spatial and temporal resolution (some nanoseconds) and they are well suited for plasma diagnosis. These experiments have furthermore in common, that the signal is produced only in the overlap volume of the two intersecting laser beams hence the spatial resolution is given by the excitation conditions present in the overlap volume. In almost, all these experiments, the variation of the plasma parameters to be measured was negligible compared to the spatial resolution, except for the E-field strength measurements in a HCD. In fact, in recent more accurate experimental studies in deuterium and hydrogen via optogalvanic spectroscopy in HCD[12,13] we have found that the E-field in front of the cathode increases, in a sheath of about 2 mm, up to 4 kV/cm. The spatial resolution was estimated using pinhole and geometrical optics resulting, in this case, in a length of 30 mm and a focal diameter of 200 μm in the overlap centre. In spite of this good value, a deep interpretation of the strong variation of the E-field demands a reliable and independent determination of the spatial resolution in this kind of experiments.

So that the aim of this paper is to determine the spatial resolution via the excitation conditions in the measurement volume with high precision based on an alternative and novel approach. To achieve this, we employ a high resolution UV camera (LaserCam-HR-UV, Coherent) to acquire spatial beam profiles, and MATLAB programs to calculate beam propagation accounting for the spatial and temporal irradiance distributions in the overlap volume. Coupled rate equations, suited for the two-photon excitation of the 1S-2S transition of atomic hydrogen, are finally used to calculate, with high spatial resolution, the three-dimensional distribution of the ionization yield for optogalvanic detection and secondarily the LIF yield distribution. The analysis of the yield distributions provides the characterization of spatial

---

[a] e-mail: concha@opt.uva.es

0021-8979/2014/116(13)/133103/8/$30.00

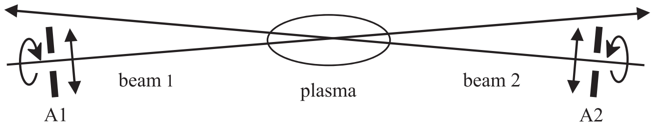

FIG. 1. Scheme of Doppler-free two-photon excitation; the irradiance distribution of the beam waists can be shaped by using different aperture diameters A1 and A2.

resolution, saturation effects, etc., for both detection schemes, which allow for a detailed comparison of optogalvanic with LIF detection in a wide range of excitation conditions. Dealing with hydrogen has the advantage that the employed atomic constants (cross sections) are precisely known; hence the obtained results are deduced from first principles.

II. TWO-PHOTON EXCITATION CONDITIONS

The laser system consists of a 10 Hz injection-seeded Q-switched Nd:YAG laser (Continuum, Powerlite) and a substantially modified optical parametric oscillator – optical parametric amplifier (OPO – OPA) system (Continuum, Mirage 500). This laser offers tunable radiation in the visible and near-IR range (426 nm to 2.12 μm). A Beta-Barium Borate (BBO) crystal converts the OPA output into tunable SLM radiation in the entire UV range from 200 nm to 300 nm by sum-frequency generation with the residual third harmonic of the Nd:YAG. The system is optimized for the 243 nm radiation, as required for the study of the 1S-2S transition of hydrogen, providing a linearly polarized laser beam up to 5 mJ pulse energy in 2.5 ns at 243 nm, with a bandwidth of about 300 MHz and excellent performance at 10 Hz repetition rate.[14]

The laser radiation is split in two beams, a complete description of a typical experimental set-up used for plasma and flame diagnostic, can be seen elsewhere.[8,12] As this work is dedicated to study the spatial resolution in the overlap volume, we just explain the main aspects of beam preparation. The selection rule of the angular momentum for two-photon absorption for the 1S-2S hydrogen transition postulates $\Delta L = 0$, this means, the two-photon excitation is only possible for the absorption of one photon out of each beam opposite circularly polarized. In our experiment (Fig. 1), each beam finally passes through an aperture and is focused (1 m focus length lens) into the overlap region.

To acquire the beam profiles in the overlap region at 243 nm, we used the high resolution UV camera, having a spectral sensitivity range from 190 nm to 355 nm. The CMOS sensor has a size of about 8.6 mm × 6.9 mm and provides 1280 × 1024 pixels of 6.7 μm × 6.7 μm. The pulse energy of each beam was reduced via polarization attenuators in order to avoid saturation (5 mJ/cm^2 with filter) of the camera. Beam waists measurements have been done with a crossing angle of about 1.53°. This particular angle comes from our experimental arrangement limitation for Doppler-free configuration.[12,13] The beam waist measurements consisted of 60 subsequent samples taken for each of the two beams, for different apertures used for the variation of the beam waist diameter and at three positions: 30 mm before, in the centre and 30 mm behind the beam overlap.

III. SINGLE SHOT CHARACTERISTICS AND BACKGROUND CORRECTION

For the basic beam waist profile analysis, the Coherent BeamView USB 4.4.2 software tools were used. Shot to shot reproducibility is analyzed comparing all single shot captures of a sequence with the average: the effective diameter (determined via 86.5% of the profile) exhibits variations smaller than 1%, while shot to shot fluctuations of the peak maximum are less than 10%, and the peak position varies less than 1 pixel. For all further analysis and calculations, we decided to use an averaged profile given by the sequence average of 60 captures.

As the beam waist is fairly small compared to the sensor size we have treated only an area of 1 mm × 1 mm corresponding to 150 × 150 pixels centred with respect to the maximum of the profile. The camera software allows for automatic background subtraction, based on recording a "background map" which counts for electronic pixel noise and present background radiation. This "background" is automatically subtracted of all the following captures of the laser beam radiation to be measured. Nevertheless, analyzing beam profiles recorded with automatic background subtraction, we noticed unacceptable change in the surrounding area of the beam profile. It is quite difficult to maintain stable background radiation, because all optical components involved in the beam preparation generate some amount of scattered radiation, and just changing the position of the laser beam shutter or the apertures A1 or A2 (Fig. 1) results in different "background maps". Therefore, we decided to use individual background correction for each profile, subtracting the average background of the area surrounding the beam profile, and define all pixel values which are smaller 0.5% of the maximum to be insignificant and put to zero. This procedure leads to well defined beam profiles surrounded by zero values, absolutely necessary in the following calculations. The background correction of one typical beam profile is shown in Fig. 2.

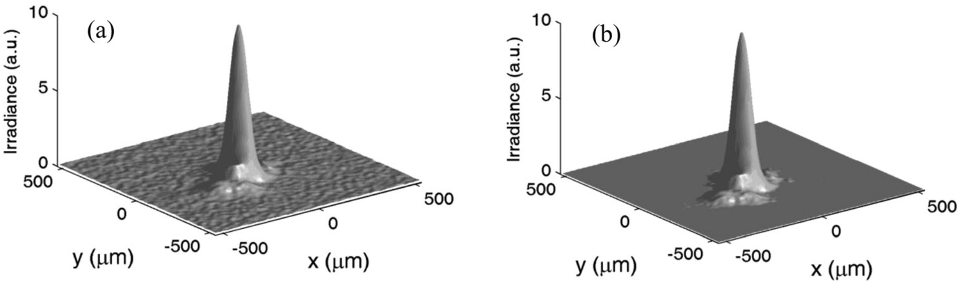

FIG. 2. Beam profile with background (**a**), after background subtraction (**b**).

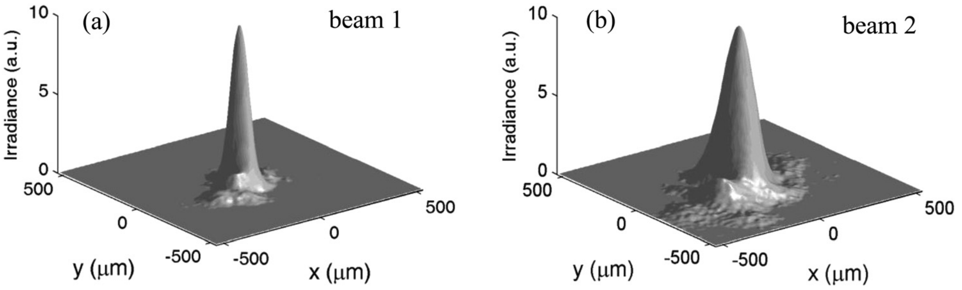

FIG. 3. Beam waist of beam 1, aperture diameter A1 = 4 mm, FWHM vertical = 107 μm, horizontal = 87 μm **(a)**; beam waist of beam 2, aperture diameter A2 = 2 mm, FWHM vertical = 174 μm, horizontal = 154 μm **(b)**.

As commonly known, the beam waists of the beams 1 and 2 depend on the apertures A1 and A2, respectively, hence it is possible to compose the overlap volume in certain limits. In order to have better pulse to pulse stability while recording two-photon absorption spectra, we always choose a narrow beam waist diameter for one of the beams (beam 1) and a larger beam waist for the other one (beam 2), as an example, see Fig. 3.

Comparing the beam waist profiles for one configuration at −30 mm before, at the centre and at 30 mm behind the beam overlap, we can state, that the FWHM of the waists does not exhibit any noticeable change. This fact allows using the beam profiles recorded in the centre of the overlap for the simulation of the beams propagation.

IV. CALCULATION PROCEDURE

The characterization of the spatial resolution provided by optogalvanic detection or LIF requires the integration of the rate equations for the two-photon resonant excitation of the 1S-2S transition generated by the laser pulse. Fig. 4 shows a simplified energy level diagram for this transition together with all the processes involved: two-photon excitation and de-excitation, ionization, and fluorescence decay.

The two-photon excitation depletes the atomic ground state density N_1 and increases the number N_2 of atoms in the excited 2S level. Collisions and even small local electric field strength cause strong coupling between the 2S and 2P levels, which are assumed to be equally populated. Hence N_2 comprises all laser excited atoms. The number density N_2 suffers from spontaneous laser induced Lyman-α emission N_f. Photo-ionization by absorbing a third laser photon creates an ion density N_i. The corresponding coupled rate equations describing the evolution of the interesting number densities produced by the irradiances of the two laser beams (E_1 and E_2) are:

$$
\begin{aligned}
\frac{dN_1}{dt} &= -N_1 c_{12} F_S[E_1(t)E_2(t)] + N_2 c_{12} F_S[E_1(t)E_2(t)] + N_2 \tau_{21}^{-1},\\
\frac{dN_2}{dt} &= N_1 c_{12} F_S[E_1(t)E_2(t)] - N_2 c_{12} F_S[E_1(t)E_2(t)]\\
&\quad - N_2 \tau_{21}^{-1} - N_2 c_i[E_1(t) + E_2(t)],\\
\frac{dN_f}{dt} &= N_2 \tau_{21}^{-1},\\
\frac{dN_i}{dt} &= N_2 c_i[E_1(t) + E_2(t)], \qquad (1)
\end{aligned}
$$

using the constants c_i for photo-ionization, c_{12} for two-photon excitation, τ_{21} counts for the life time of the two-photon excited level and the spectral factor $F_s \leq 1$ is related to the spectral widths of laser and absorption profiles.

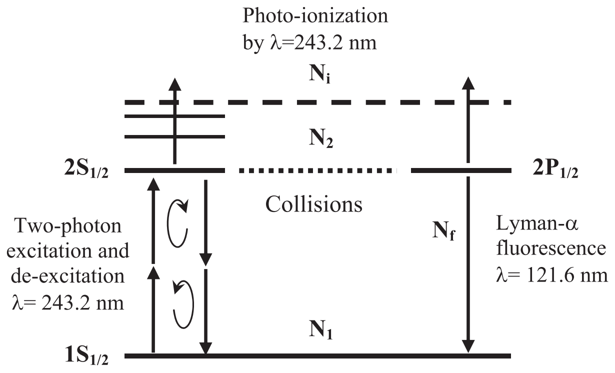

FIG. 4. Simplified energy level diagram for the 1S - 2S transition with relevant processes involved: two-photon excitation and de-excitation, ionization and fluorescence decay.

Based on the ionization cross-section 4.7 × 10^{-22} m^2,[15] the photo-ionization constant has the value: $c_i = 5.8 \times 10^{-3}$ $(MW/cm^2)^{-1} ns^{-1}$.

The two-photon excitation constant $c_{12} = 2.9 \times 10^{-5}$ $(MW/cm^2)^{-2} ns^{-1}$ includes the two-photon excitation cross-section $\sigma_{12} = 1.43 \times 10^{-43}$ m^4,[16] and the statistical factor G = 1 owing to coherent SLM laser radiation. Furthermore, the excitation constant accounts for the spectral laser bandwidth (FWHM δv_L) and the absorption profile (FWHM δv_A). The SLM laser radiation has Gaussian distribution ($\delta v_L = 0.35$ GHz), and for the present approximation, we assume also a Gaussian profile for the two-photon absorption. The convolution of these Gaussian profiles depends on the relation of the bandwidths δv_A and δv_L. Therefore, we introduce the spectral factor Fs, hence Fs = 1 holds for $\delta v_A = \delta v_L$, and it decreases with increasing absorption width, see Fig. 5.

The life time of the 2P level is 1.6 ns,[17,18] and the long lifetime of the metastable 2S state is strongly reduced by mixing of the 2S-2P states in presence of local electric field strength and due to collisional quenching from 2S to 2P. The lifetime reduction for the 2S state can be estimated[18] and gives, e.g., about 64 ns for field strength of 3 $kVcm^{-1}$. Measurements of two-photon induced Lyman-α fluorescence[10] performed in feasibility study at the plasma-generator PSI-1 (Ref. 19) revealed a life time of about 8 ns for deuterium plasma of neutral densities and electron densities of about 10^{12} cm^{-3}. As our HCD does not reach such densities, we will use for our calculations a somehow

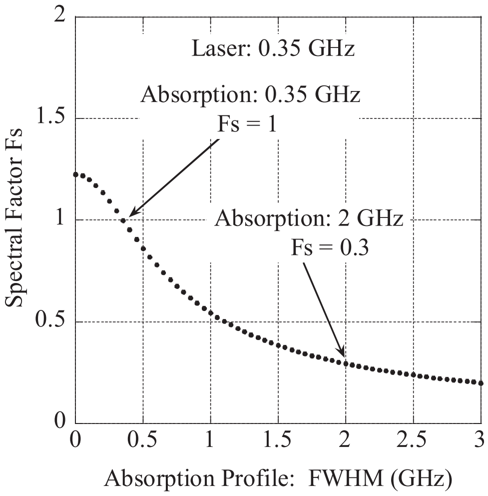

FIG. 5. Spectral factor F_s versus FWHM of the absorption profile. $F_s = 1$ corresponds to equal Gaussian profiles for absorption and laser bandwidth with a FWHM of 0.35 GHz.

underestimated larger lifetime $\tau_{21} = 10$ ns. However, as the laser pulse duration of 2.5 ns (Fig. 6) is small compared to this estimated lifetime, the corresponding uncertainty on the results of the calculations is quite small. This will be discussed in more detail in the following paragraph. Stronger mixing and quenching of the 2S-2P states have been estimated only for fusion plasma conditions.[20]

The electron ion recombination is not considered, because it is a much slower process that takes place on the scale of microseconds, negligible therefore compared to the lifetime τ_{21}. Quenching of the 2S and 2P levels into levels with higher quantum numbers can be incorporated in the rate equations if necessary. The photo-ionization of all other excited upper level densities present in the plasma is laser frequency independent, and leads only to a very small constant background signal, which is proportional to the sum of the laser beam irradiances.

Integration of the rate equations requires knowledge of the temporal and spatial irradiance distribution in the both beam waists. The smooth temporal pulse shape S(t) of the SLM laser radiation allows to factorize spatial and temporal dependences of the irradiance

$$E(x,y,z,t) = E(x,y,z)S(t). \quad (2)$$

Because of the short length of the overlap volume the variation of the irradiances for each of the beams in the propagation direction z, can be neglected as above stated. This means that the recorded beam profiles (pixel size: $\Delta x = 6.7\,\mu m \times \Delta y = 6.7\,\mu m$) are converted into irradiance matrices E $(\Delta x_n, \Delta y_m)$ counting for specific pulse energies and the laser pulse shape S(t):

$$E_i(x,y,z) = E_i(\Delta x_n, \Delta y_m) \text{ beam-index } i = 1, 2$$
$$\text{and for all } z \text{ in the overlap region.} \quad (3)$$

The spatial overlap can be simulated for a wide range of experimental conditions using combinations of various beam waists and different pulse energies. However, in our case, the two-counter propagating beams are always crossing at a small angle of 1.53° in the horizontal plane. The crossing angle and the resulting overlap volume are implemented in the calculations, the irradiance matrices are displaced horizontally every 500 μm while propagating in z direction, starting, e.g., 15 mm before and ending 15 mm behind the overlap centre. The overlap region is simulated therefore by 61 transversal slices, each representing a specific irradiance overlap of the two beams for a propagation length of 500 μm, while the irradiance varies in time intervals $\Delta t = 50$ ps with the temporal laser pulse shape:

$$E_1(\Delta x_n, \Delta y_m)\,S(\Delta t_k)\,E_2(\Delta x_i, \Delta y_j)\,S(\Delta t_k). \quad (4)$$

The temporal laser pulse shape was measured with a fast photodiode and it is approximated by two semi-Gaussian functions with a total FWHM = 2.5 ns, the rising pulse has a FWHM of 2 ns and the falling slope has a FWHM of 3 ns, see Fig. 6.

The overlapping irradiance matrices (Eq. (4)) for all transversal slices and their temporal variation, allow the numerical integration of the rate equations (Eq. (1)) for tiny volume elements (cells), all having the same size of $\Delta x = 6.7\,\mu m \times \Delta y = 6.7\,\mu m \times \Delta z = 500\,\mu m$. Accounting only for the laser induced changes, we start to resolve the rate equations with a fixed and homogenous ground state number density of $N_1 = 10^{13}\,cm^{-3}$,[7] hence all results are scaling linearly with variations of this ground state density. The integration finishes with the end of the laser pulse and reveals for each cell, the number of generated ions (Ion Yield = YN_{Ion}), the number of already emitted laser induced photons YN_f, and the remaining number of laser excited atoms YN_2, which are expected to decay via fluorescence in absence of inelastic collisions. The number of all laser induced photons (LIF Yield = YN_{LIF}) emitted from the two photon excited level is therefore, the sum of YN_f and YN_2. The yield distributions YN_{Ion} and YN_{LIF} in the entire overlap region are the desired results, which will be analyzed below.

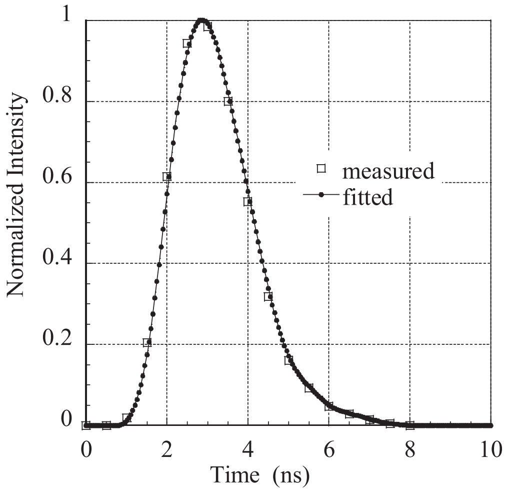

FIG. 6. Temporal pulse shape of the tunable SLM laser radiation generated by the OPO. The values of the semi-Gaussian fit ($\Delta t = 50$ ps) are used for numerical integration of the rate equations.

V. RESULTS

The yield distributions, the corresponding spatial resolution and the depletion of the ground state density depend strongly on experimental parameters, especially on the irradiance distributions of the two-counter propagating beams, i.e., on the beam profiles and the pulse energy chosen for each beam. The primary aim of the following analysis is to reveal some important characteristics of yield distributions that correspond to the experimental conditions used for the recent local electric field strength measurements.[12,13] In these experiments, and in the following calculations, a beam with a narrow beam waist is combined with a broader one, like beam 1 and beam 2 shown in Fig. 3, and both beams have equal pulse energy. Therefore, the peak irradiance of beam 1 is about three times larger than that of beam 2. Furthermore, the peak irradiance of beam 1 is always used as a characteristic quantity in the following analysis. In order to study the impact of the spectral factor two different F_s values will be used. $F_s = 1$ accounts for a two-photon absorption profile equal to the laser bandwidths, and $F_s = 0.3$ corresponds to a two photon absorption profile which is about six times broader than the laser bandwidths. For simplification, the results obtained for Ion yield distributions will be indicated in all figures by "ION" (related to optogalvanic detection) and LIF yield distributions by "LIF."

A. Overview

Fig. 7 visualizes the calculated 3-dimentional yield distributions obtained for 40 μJ pulse energy in both beams. Fig. 7(a) shows the fluorescence yield LIF and Fig. 7(b) the Ion yield in the central area of the overlap volume, represented by five transversal slices separated 2.5 mm each other. The yield scale refers to the ground state density of $N_1 = 10^{13}\,\mathrm{cm}^{-3}$, and the ground state depletion is well below 10%. The size of each slice represents a section of only 200 μm × 200 μm, which correspond to 60 × 60 pixels of the camera. The peak irradiance of beam 1 is about 142 MW/cm^2, and one third for the broader profile. Obviously, the spatial resolution provided by optogalvanic detection (i.e., the Ion Yield) is remarkably better than that of LIF detection.

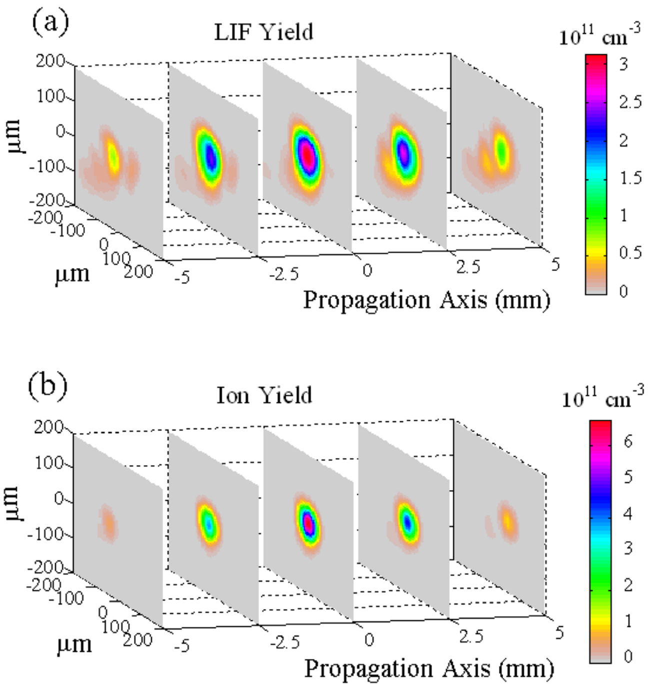

FIG. 7. Transversal slices of the fluorescence yield LIF (**a**), and the Ion yield (**b**) for 40 μJ pulse energy in both beams and a spectral factor $F_s = 0.3$. Each slice represents 3600 cells according to the camera pixel size 6.7 μm × 6.7 μm and a propagation length of 500 μm.

B. Total yields and spatial resolution

Fig. 8(a) shows the results obtained for the total Ion yield and total LIF yield for a large variation of pulse energies and irradiances. The total yield is the integral of the yield distribution over the entire overlap volume. Both beams are set to have equal pulse energy; hence the maximum irradiance of beam 1 is about three times that of beam 2. The corresponding pulse energies are varying from 2.5 μJ

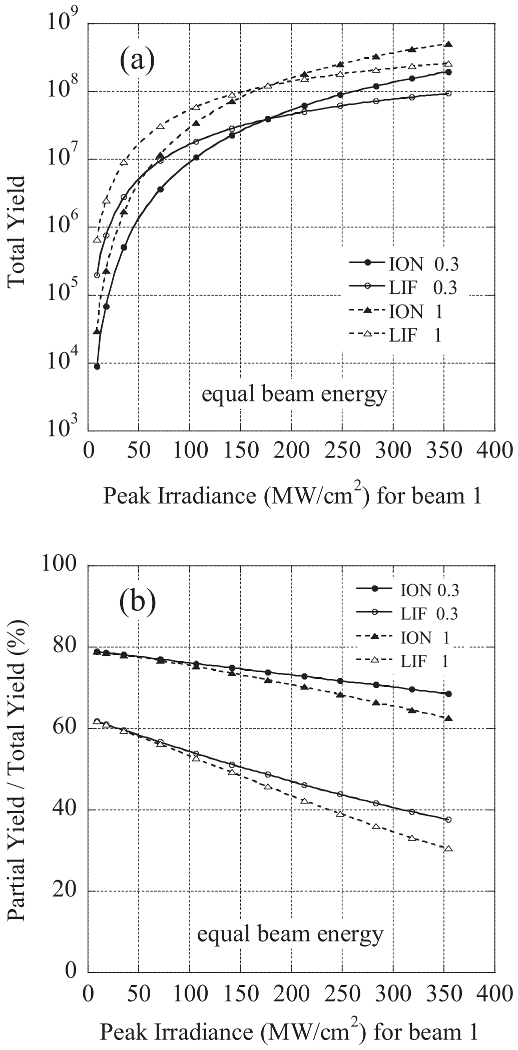

FIG. 8. Comparison of total Ion and LIF yields versus maximum irradiance of beam 1 for two spectral factors $F_s = 1$ and $F_s = 0.3$ as indicated (**a**). The corresponding ratios—partial yield/total yield—characterize the spatial resolution (**b**). The partial yield integrals cover the central area of the overlap: 100 μm × 100 μm and a length of 10 mm.

to 120 μJ. The two upper curves correspond to the Ion Yield and LIF yield obtained for a spectral factor $F_s = 1$, while the two lower curves are calculated for a spectral factor $F_s = 0.3$. Obviously at low irradiance, the Ion yield is small compared to LIF yield, but the Ion yield increases much faster with increasing irradiances and prevails LIF yield above 180 MW/cm^2, because the photo-ionization results in a depletion of the two-photon excited level causing finally the depletion of the ground state density.

The comparison of the total yields with partially integrated yields allows characterizing the spatial resolution more specifically. The yield integrals, over the entire overlap volume (536 μm × 536 μm × 30 mm length), give the total yields, and the partial yields are analyzed in two steps. In a first step, the partial yields are calculated by integrating the yields over a selected reduced area perpendicular to the propagation direction centred along the axis of the entire overlap volume, and in a second step the length of the partial integral is reduced furthermore, so that the reduced partial integral changes about 1%. Fig. 8(b) shows the corresponding ratios of the partial yields divided by the total yields, given as percentage, obtained for a tiny central area of the probe volume of only 100 μm × 100 μm and a length of 10 mm. Larger values correspond to better spatial resolution. The optogalvanic detection reveals an exceptionally high spatial resolution, because for $F_s = 1$ ($F_s = 0.3$) and irradiances up to 100 MW/cm^2 (150 MW/cm^2) more than 75% of the optogalvanic signal is created in this tiny central area of the probe volume. For $F_s = 0.3$ and irradiances up to 300 MW/cm^2, the ratio is still about 70%. Similar percentages for LIF signals are only obtained, if the central area is increased to be 140 μm × 140 μm × 14 mm, hence the probe volume would be about twice as large for LIF detection compared to optogalvanic detection. In general, the spatial resolution for LIF is remarkably lower and becomes worse with increasing irradiance. However, the spatial resolution of LIF detection can be improved only perpendicular to the observation direction implementing a spatial filter (e.g., a rectangular aperture) for the image of overlap volume.[3,21,22] The spatial resolution provided by our experimental set-up can be even higher if both beams have similarly tight waists as beam 1 in Fig. 3. In this case, the optogalvanic detection can provide a spatial resolution of about 75 μm × 75 μm × 8 mm using lenses of 1 m focal length.

C. Ground state depletion and spectral factor

First, we contemplate the depletion of the ground state density (N_1) and the two-photon excited level density (N_2) as a consequence of increasing irradiance for a spectral factor $F_s = 0.3$. Fig. 9 shows a horizontal row of the 3D yield matrixes located in the centre of the overlap volume, which represents the yield per cell (6.7 μm × 6.7 μm × 500 μm). Fig. 9(a) corresponds to equal pulse energy of 40 μJ for both beams, and the maximum irradiance of beam 1 is about 142 MW/cm^2. Fig. 9(b) shows the results obtained for 120 μJ in both beams and a maximum irradiance 426 MW/cm^2 which exhibits a strong depletion of N_1 due to two-photon absorption and subsequent photo-ionization causing a broad plateau with a wide central dip in the LIF yield. With increasing irradiance the dip will show up even more pronounced.

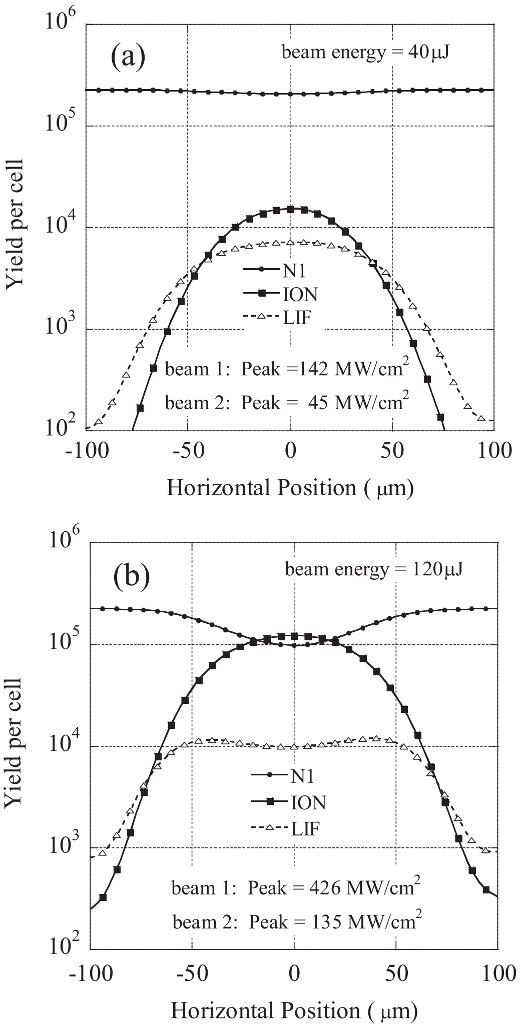

FIG. 9. Demonstration of ground state depletion. Ion yield and LIF yield per cell are plotted versus the horizontal position in the centre of the overlap volume for a spectral factor $F_s = 0.3$ for moderate pulse energy **(a)**, and three times larger pulse energy **(b).**

A detailed analysis of depletion effects reveals some interesting insight. For maximum irradiances below 60 MW/cm^2 in beam 1 saturation effects due to ground state depletion and photo-ionization are negligible because the entire LIF yield (Fig. 7) varies with square of the maximum irradiance. However, with increasing irradiance the photo-ionization starts to eat up the 2S 2P levels, hence LIF suffers already depletion, although the ground state depletion is still negligible. On the other hand, the subsequent ionization of the two-photon excited level causes that the Ion yield varies with the third power up to irradiances of 150 MW/cm^2 in beam 1 and starts to suffer only from ground state depletion for larger irradiances. This holds for both spectral factors F_s equal to 1 and 0.3.

Now, we analyse how the spectral factor F_s influences the excitation conditions. Fig. 10 reveals a horizontal row of the yield matrixes calculated for a spectral factor $F_s = 1$ and for reduced pulse energy of 25 μJ in both beams. The corresponding maximum irradiance is 89 MW/cm^2, and the

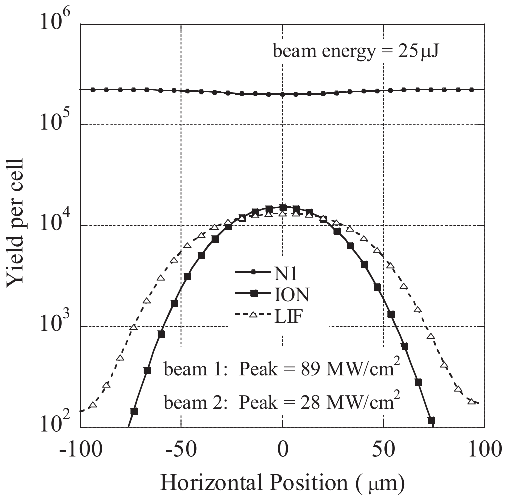

FIG. 10. Ion and LIF yield per cell are plotted versus the horizontal position in the centre of the overlap volume for a spectral factor Fs = 1. Pulse energy of 25 μJ in both beams is chosen in order to obtain similar excitation conditions as in Fig. 9(a).

ground state depletion in the centre is exactly the same as in Fig. 9(a). Obviously, the yields are different as consequence of the different spectral factors. The Ion yield differs only by about 1%, while the fluorescence yield is a factor 1.8 larger for $F_s = 1$. Hence, one can draw the conclusion that broader two-photon absorption profiles are favourable for optogalvanic detection and lead to disadvantage for LIF detection.

This example illustrates the importance of the spectral factor in the case of optogalvanic spectroscopy: broader two-photon absorption profiles can be measured with remarkably higher irradiances than narrow ones, and the Ion yield takes advantage due to the depletion of the two-photon excited density N_2, hence the spatial resolution depends very little on the two-photon absorption profile and the pulse energy, and the signal magnitude can be maintained using larger pulse energy for broader profiles.

Finally, we like to comment the influence of the time constant on the results. For all calculations, an underestimated time constant $\tau_{21} = 10$ ns has been used. However, a precise determination of the time constant would require a detailed knowledge of the collisional transfer from 2S to 2P and furthermore the 2S-2P mixing due to local electric field strength. Nevertheless, a larger time constant has only little effect on the previously discussed results, because the laser pulse duration of 2.5 ns is small compared to the time constant. In order to study the effect of a larger time constant (less perturbations and level mixing) on the results, calculations were conducted with $\tau_{21} = 50$ ns, $F_s = 0.3$ and 40 μJ pulse energy of both beams. Comparison with the results of Fig. 9(a) reveals for the central position that the ground state depletion remains negligible and increases only by 1%, while the Ion yield increases by 6% and the LIF yield decreases by 13%, because a slower radiative decay implies an accumulation in the two-photon excited 2S level and favours photo-ionization.

VI. CONCLUSIONS

We have calculated and analyzed with high spatial resolution the yield distributions for the Ion yield (optogalvanic detection) in the overlap region for typical experimental conditions, recently used in our laboratory for local E-field strength measurements in the cathode fall region in hollow cathode discharges. These calculations reveal that the measurements provide an exceptional high resolution because more than 75% of the total Ion yield is generated in a central area of only 100 μm × 100 μm having a length of 10 mm; four times better than estimated so far. However, the results obtained in this study are independent of experimental details and of the embedment of the laser beams in the discharge, and are valid in general for SLM pulsed laser radiation of some ns duration. The calculations are based on the measured irradiance distribution (pixel size 6.7 μm × 6.7 μm) in the beam waists of the overlapping laser beams, used for two-photon excitation of the 1S-2S hydrogen transition; and the integration of the rate equations for the temporal laser pulse. Atomic hydrogen has the advantage that the employed atomic constants (cross sections) are precisely known; hence the obtained results are deduced from first principles. The rate equations reveal laser induced changes accounting for the resonant two-photon absorption, photo-ionization and fluorescence decay. Calculations, for various irradiances, which depend on laser beam preparation and pulse energies, allow characterizing the spatial resolution, saturation and the influence of the spectral width of the two-photon absorption profile on Ion yield and additionally on LIF yield. A comparison of Ion yield and LIF yield reveals details of general interest. In a wide range of excitation conditions, the spatial resolution for LIF detection without spatial filtering is worse by a factor of about two. LIF detection suffers at much smaller irradiances from depletion than optogalvanic detection, because even if the ground state depletion is still negligible, the photo-ionization already depletes the two-photon excited level and reduces the LIF yield. This favours the optogalvanic detection because the measurements can be performed at larger irradiances without losing the high spatial resolution. A similar advantage for optogalvanic detection holds for two-photon absorption profiles broader than the laser bandwidth (0.35 GHz), because the two-photon excitation rate decreases while the ionization rate remains the same. Therefore, optogalvanic detection is perfectly suited for local electric field strength measurements which reveal a strong broadening of the shifted 2S Stark components.[12,13] Under usual experimental conditions, the duration of the laser pulse (2.5 ns) is small compared to the fluorescence decay time; hence a detailed knowledge is not essential for the conclusions drawn in this study. If necessary, the rate equations can be extended to other two-photon transitions, quenching and branching rations can be included. This type of calculations opens the possibility that future measurements, e.g., of strongly varying local electrical field strength using optogalvanic or LIF detection can be optimized with respect to beam waist preparation and selected pulse energies in order to achieve substantially improved results and reliable interpretation of spectra. In those experiments, the irradiance distribution and related yield distributions of the measurement volume can be monitored in situ.

ACKNOWLEDGMENTS

The authors wish to thank Mr. S. González for the technological support. The present work was supported by the DGICYT (Ministerio de Educación Cultura y Deporte) Contract Reference No. FIS2007-62604 and by DGICYT (Ministerio de Economía y Competitividad) Contract Reference No. ENE2012-35902 and FEDER funds.

[1] W. Demtröder, *Laser Spectroscopy* (Springer, Berlin, Heidelberg, 1996).

[2] K. Muraoka and M. Maeda, *Laser-Aided Diagnostics of Plasmas and Gases* (IOP Publishing Ltd, 2001).

[3] J. Amorim, G. Baravian, and J. Jolly, J. Phys. D: Appl. Phys. **33**, R51 (2000).

[4] K. Danzmann, K. Grützmacher, and B. Wende, Phys. Rev. Lett. **57**, 2151 (1986).

[5] M. Steiger, K. Grützmacher, and A. Steiger, in *15th Conference Spectral Line Shapes*, edited by J. Seidel (AIP, Melville, New York, 2000).

[6] R. Dux, K. Grützmacher, M. I. de la Rosa, and B. Wende, Phys. Rev. E **51**, 1416 (1995).

[7] A. B. Gonzalo, M. I. de la Rosa, C. Pérez, S. Mar, and K. Grützmacher, Plasma Sources Sci. Technol. **13**, 150 (2004).

[8] K. Grützmacher, M. I. de la Rosa, A. B. Gonzalo, M. Steiger, and A. Steiger, Appl. Phys. B **76**, 775 (2003).

[9] M. I. de la Rosa, C. Pérez, K. Grützmacher, A. B. Gonzalo, and A. Steiger, Plasma Sources Sci. Technol. **15**, 105 (2006).

[10] C. Seiser, "Measurement of two-photon absorption laser-induced lyman-α fluorescence: A diagnostic for number densities of hydrogen isotopes in magnetically confined fusion plasmas," Ph.D. thesis, Technischen Universität Berlin (1998).

[11] M. Gemišić Adamov, A. Steiger, K. Grützmacher, and J. Seidel, Phys. Rev. A **75**, 013409 (2007).

[12] M. I. de la Rosa, C. Pérez, K. Grützmacher, and L. M. Fuentes, Plasma Sources Sci. Technol. **18**, 015012 (2009).

[13] C. Pérez, M. I. de la Rosa, and K. Grützmacher, Eur. Phys. J. D **56**, 369 (2010).

[14] M. I. de la Rosa, C. Pérez, K. Grützmacher, D. García, and A. Bustillo, J. Phys.: Conf. Ser. **274**, 012088 (2011); available at http://iopscience.iop.org/1742-6596/274/1/012088.

[15] L. Holtgreven, *Plasma Diagnostics* (North-Holland Publishing Company, Amsterdam, 1968).

[16] F. Bassani, J. J. Forney, and A. Quattropani, Phys. Rev. Lett. **39**, 1070 (1977).

[17] R. Loudon, *The Quantum Theory of Light* (Clarendon Press, Oxford, 1973).

[18] B. Salpeter, *Quantum Mechanics of One and Two-Electron Atoms* (Plenum Publishing Corporation, New York, 1977).

[19] A. Steiger, K. Grützmacher, Ch. Seiser, M. I. de la Rosa, and U. Johannesen, in *14th Conf. Spectral Line Shapes, Conference Proceedings*, edited by R. Herman (AIP, New York, 1999), p. 467.

[20] D. Voslamber, "Determination of neutral particle density and magnetic field direction from laser-induced Lyman-α fluorescente II: Two-photon excitation," Rep. EUR.CEA.-FC-1387, CEN Cadarache, St. Paul-lez Durance, France (1990).

[21] U. Czarnetzki, J. Phys IV France **7**, C4-175 (1997).

[22] S. Mazouffre, P. Vankan, R. Engeln, and D. C. Schram, Phys. Plasmas **8**, 3824 (2001).